Article:

Key Points:
- New detailed non-LTE OH(v) model is applied to analyze SABER nighttime Meinel band emissions
- Novel two-channel O(^{3}P) retrieval technique uses SABER nighttime 2.0- and 1.6-micrometer radiances
- New retrievals reconcile large differences with O(^{3}P) derived from other airglows

Supporting Information:
- Supporting Information S1
- Data Set S1
- Data Set S2
- Data Set S3

Correspondence to:
P. A. Panka,
peter.a.panka@nasa.gov

Atomic Oxygen Retrieved From the SABER 2.0- and 1.6-μm Radiances Using New First-Principles Nighttime OH(v) Model

Peter A. Panka[1] [ID], Alexander A. Kutepov[1,2] [ID], Ladislav Rezac[3] [ID], Konstantinos S. Kalogerakis[4] [ID], Artem G. Feofilov[5] [ID], Daniel Marsh[6] [ID], Diego Janches[1] [ID], and Erdal Yiğit[7] [ID]

[1]NASA Goddard Space Flight Center, Greenbelt, MD, USA, [2]The Catholic University of America, Washington, DC, USA, [3]Max Planck Institute for Solar System Research, Göttingen, Germany, [4]Center for Geospace Studies, SRI International, Menlo Park, CA, USA, [5]Laboratoire de Météorologie Dynamique, IPSL, Sorbonne Université, École Polytechnique, CNRS, Palaiseau, France, [6]National Center for Atmospheric Research, Boulder, CO, USA, [7]Department of Physics and Astronomy, George Mason University, Fairfax, VA, USA

Abstract The recently discovered fast, multiquantum OH(v)+O(^{3}P) vibrational-to-electronic relaxation mechanism provided new insight into the OH(v) Meinel band nighttime emission formation. Using a new detailed OH(v) model and novel retrieval algorithm, we obtained O(^{3}P) densities in the nighttime mesosphere and lower thermosphere (MLT) from the Sounding of the Atmosphere using Broadband Emission Radiometry (SABER) 2.0- and 1.6-μm radiances. We demonstrate how critical the new OH(v) relaxation mechanism is in the estimation of the abundance of O(^{3}P) in the nighttime MLT. Furthermore, the inclusion of this mechanism enables us to reconcile historically large discrepancies with O(^{3}P) results in the MLT obtained with different physical models and retrieval techniques from WIND Imaging Interferometer, Optical Spectrograph and Infrared Imager System, and Scanning Imaging Absorption Spectrometer for Atmospheric Chartography observations of other airglow emissions. Whereas previous SABER O(^{3}P) densities were up to 60% higher compared to other measurements the new retrievals agree with them within the range ($\pm$25%) of retrieval uncertainties. We also elaborate on the implications of this outcome for the aeronomy and energy budget of the MLT region.

Plain Language Summary The recently discovered fast hydroxyl-atomic oxygen relaxation mechanism provided new insight into the mesospheric emission formation. Using a new hydroxyl (OH) model and retrieval algorithm, we obtained atomic oxygen concentration in the nighttime mesosphere and lower thermosphere (MLT) from the SABER OH radiances. We demonstrate how critical this new relaxation mechanism is in the estimation of the abundance of atomic oxygen in the nighttime MLT. Furthermore, the inclusion of this mechanism enables us to reconcile historically large discrepancies with atomic oxygen results in the MLT obtained with different physical models and retrieval techniques from WINDII, OSIRIS, and SCIAMACHY observations of other airglow emissions. Whereas previous SABER atomic oxygen densities were up to 60% higher compared to other measurements, the new retrievals agree with them within the range ($\pm$25%) of retrieval uncertainties. We also elaborate on the implications of this outcome for the aeronomy and energy budget of the MLT region.

1. Introduction

Atomic oxygen, O(^{3}P), plays a crucial role in the physics, chemistry, and energy budget of the mesosphere and lower thermosphere (MLT; Brasseur & Solomon, 2005). It is one of the most abundant trace gases in this region of the atmosphere with a chemical lifetime varying from seconds at 50 km to months at 100 km. Formed mostly in the thermosphere during the day by photolysis of molecular oxygen, O$_2$, and, ozone, O$_3$, O(^{3}P) is transported downward through both diffusion and advection, reaching peak nighttime concentrations at altitudes around 96 km. Recombination of atomic oxygen is an important heating mechanism while the dominant radiative cooling of the MLT is caused by the 15-μm radiation of carbon dioxide, CO$_2$, excited by collisions with O(^{3}P). Finally, reliable retrievals of temperature (Kutepov et al., 2006; López-Puertas & Taylor, 2001), ozone (Kaufmann et al., 2003; Smith et al., 2008), and other constituents also strongly depend on the knowledge of atomic oxygen.

The O(^{3}P) densities in the MLT are usually derived from airglow observations. Recent results rely on the measurements of O(^{1}S) green line and hydroxyl, OH, (8–3) band emissions by WINDII (WIND Imaging Interferometer) on the Upper Atmosphere Research Satellite (Russell et al., 2005), O$_2$ A-band emissions by OSIRIS (Optical Spectrograph and Infrared Imager System) on the Odin satellite (Sheese et al., 2011), O(^{1}S) green line emissions by the SCIAMACHY (Scanning Imaging Absorption Spectrometer for Atmospheric Chartography) instrument on Envisat (Kaufmann et al., 2014), and OH(9–7) and OH(8–6) band emissions by the SABER (Sounding of the Atmosphere using Broadband Emission Radiometry) instrument onboard the Thermosphere Ionosphere Mesosphere Energetics and Dynamics satellite (Mlynczak et al., 2013; Smith et al., 2010, hereafter SABER-2013). Kaufmann et al. (2014), however, showed that WINDII, OSIRIS, and SCIAMACHY O(^{3}P) densities in the MLT differ by not more than 20%, while SABER-2013 O(^{3}P) is up to 60% higher compared to those results.

The significant differences between SABER nighttime O(^{3}P) in the MLT and results of other studies stimulated revision of both the OH(v) emission model and retrieval algorithm applied to SABER measurements. The new, detailed model of the nighttime OH(v) Meinel band emissions developed in the framework of this study was recently presented by Panka et al. (2017). In this paper, we outline this model focusing on its differences with the model applied in the previous SABER O(^{3}P) analysis. We also provide a description of a new retrieval technique and present updated nighttime O(^{3}P) densities in the MLT retrieved from SABER OH radiances. We compare the derived O(^{3}P) densities to previous SABER results as well as to other independent measurements. Finally, we discuss the implication of the lower O(^{3}P) densities for the MLT aeronomy and energy budget.
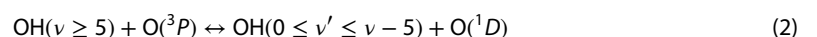
2. Model and Retrieval Algorithm

The nighttime SABER-2013 O(^{3}P) retrievals utilized volume emission rates (VERs) derived from the SABER OH 2.0-μm channel and an OH(v) model, which included OH chemical production H+O$_3$ →OH(v)+O$_2$ in the $v = 8$ and 9 states, spontaneous emission, and collisional quenching by N$_2$, O$_2$, and O(^{3}P). For these retrievals, Mlynczak et al. (2013) applied a much lower rate coefficient for OH($v = 8, 9$)+O(^{3}P) quenching relative to the measurements reported in Kalogerakis et al. (2011). At the time Mlynczak et al. (2013) argued that higher rates led to a significant enhancement in the retrieved O(^{3}P). Nevertheless, even the empirically lowered rates did not bring the SABER-2013 O(^{3}P) into agreement with other measurements as demonstrated in Kaufmann et al. (2014).

The new non-LTE (for nonlocal thermodynamic equilibrium) model (Panka et al., 2017) of the nighttime MLT OH(v) emissions accounts for the most up-to-date laboratory and theoretical data on the chemical production, loss, and collisional relaxation of mesospheric OH(v). It accounts for 10 vibrational levels with $v = 0$–9, explicitly including the ground vibrational state, usually neglected (see, e.g., Xu et al., 2012), but required by the particle conservation principle, and solves the system

$$\sum_{v'} R_{vv'} n_{v'} = f_v P_{OH} \tag{1}$$

Here $R_{vv'}$ are total rate coefficients of radiative and collisional transitions from level v to v' calculated following corresponding selection rules (see Kutepov et al., 1998, and Gusev & Kutepov, 2003, for general non-LTE problem formalism used in the ALI-ARMS code package, Feofilov & Kutepov, 2012, applied in this work), plus chemical removal rates of each OH(v). Further, n_v is the total population of vibrational level v and the right side of (1) are chemical production terms, with the total OH production rate P_{OH} and branching ratios f_v. Spin and rotational LTE were assumed in this study. Additionally, the OH emissions are optically thin and the absorption of photons in the OH bands emitted at other altitudes or those of upwelling flux from the lower atmosphere has negligible impact. As a result the vibrational non-LTE problem (1) is local for each altitude which significantly simplifies its solution.

The model of Panka et al. (2017) is the first one which accounts for the new vibrational relaxation pathway of OH(v) by collisions with O(^{3}P) atoms

$$OH(v \geq 5) + O(^3P) \leftrightarrow OH(0 \leq v' \leq v - 5) + O(^1D) \tag{2}$$

suggested by Sharma et al. (2015) and later studied in the laboratory experiments by Kalogerakis et al. (2016). This *essential multiquantum vibrational-to-electronic relaxation process* removes at least five vibrational quanta
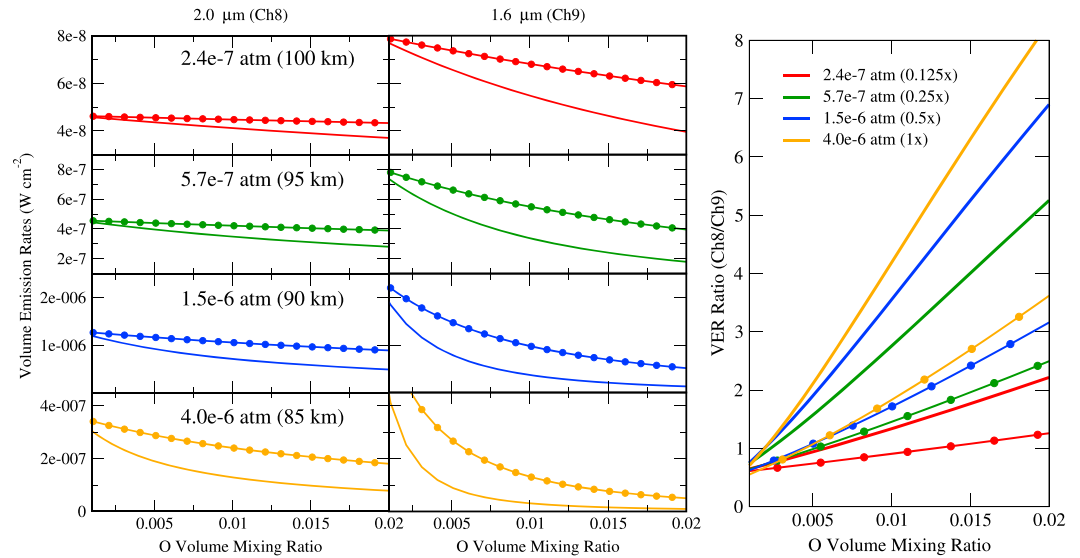
Figure 1. (left) Volume emission rate dependence on atomic oxygen density for SABER channel 8 and channel 9 at four different pressure levels. (right) Ratios of volume emissions rates (Ch8/Ch9) at the respective pressure levels. Red - 2.4e-7 atm (scaled by 0.125); Green - 5.7e-7 atm (scaled by 0.25); Blue - 1.5e-6 atm (scaled by 0.5); Green - 4.0e-6 atm (not scaled). Solid - OH non-LTE model with reaction (2); Solid with circles - OH non-LTE model without reaction (2).

in OH($v \geq 5$)+O(^{3}P) collisions and provides an efficient redistribution of the OH(v) energy from higher vibrational levels to lower ones. Compared to previous models, the new model reproduced the OH(v) population distributions derived from the ground-based (Cosby & Slanger, 2007) and space-based (Migliorini et al., 2015) observations of Meinel bands as well as the altitude profiles of the VER ratios for the OH limb emissions measured by SABER. Additionally, accounting for the transfer of OH(v) energy to the $CO_2(v_3)$ via the reaction chain OH(v) $\Rightarrow$ O(^1D) $\Rightarrow$ $N_2(v)$ $\Rightarrow$ $CO_2(v_3)$ resolved the long-standing unexplained strong 4.3-μm emissions measured by SABER (see Panka et al., 2017, for details).

The ability of the new model to reproduce the relative distribution of SABER measured VERs stimulated us to develop a novel O(^{3}P) retrieval approach, described below. SABER observes the OH Meinel band emissions in two near-infrared channels: channel 8 is sensitive to the 2.0 μm $v = 9v$ $v' = 7$ and $v = 8 \rightarrow v' = 6$ band emissions, while channel 9 is dominated by the $v=5 \rightarrow v'=3$ and $v=4 \rightarrow v'=2$ band emissions around 1.6 μm. VERs for each channel can be presented as

$$VER = [OH] \sum_v A_{v,v'} p_v \qquad (3)$$

where p_v=[OH(v)]/[OH] is the probability of the OH molecule to be in the vibrational state v, [OH]=$\sum_v n_v$ is the total OH density, and $A_{v,v'}$ are the Einstein coefficients for bands contributing to measured emission. It follows from this expression that the ratio of VERs for channels 8 and 9 is independent on [OH]. Additionally, one may see from (1) that the ratio of VERs depends on the branching ratios f_v, but is also independent of the total OH chemical production rate. However, the ratio will depend on collisional quenching rates and chemical loss rates which comprise the $R_{vv'}$ coefficients of system (1). The latter makes the VER ratios dependent on the OH colliding partner (N_2, O_2, and O(^{3}P)) densities.

In Figure 1 we show results of our study of VER and VER ratio dependences on the O(^{3}P) for various pressure levels of two cases with extremely different total loss of OH($v\geq 5$): when reaction (2) in our OH non-LTE model is turned on (solid lines) and off (solid lines with circles). When reaction (2) is turned off, chemical quenching of OH(v) by O(^{3}P) is still active, with a rate of 5×10^{-11} cm^3/s which is consistent with Mlynczak et al. (2013), see Table 1 of Panka et al. (2017). When reaction (2) is turned on, OH($v\geq 5$) experiences additional quenching with a rate coefficient of 2.3×10^{-10} cm^3/s (Sharma et al., 2015). We used for this study atmospheric inputs taken from the Whole Atmosphere Community Climate Model (Marsh et al., 2013).

It can be observed in Figure 1 that VERs for channel 9 (middle panel) are more sensitive to atomic oxygen than those of channel 8 (left panel) in both cases when reaction (2) is turned on and off. This stronger sensitivity is a

result of OH(v) collisions with O(^{3}P) dominating in the steady state equation for OH($v = 4$ and 5) over the weak chemical production and quenching by O$_2$. Opposite to this, chemical production and O$_2$ quenching are the dominant processes for OH($v = 8$ and 9), governing populations of these levels. As a result these populations exhibit weaker dependence on O(^{3}P).

When reaction (2) is on, the emission of these high vibrational levels OH($v = 8$ and 9) is only slightly stronger influenced by collisions with O(^{3}P) notwithstanding the relatively high rate coefficient of this reaction (2.3×10^{-10} cm^3/s). This effect is, however, much more prominent in the OH VERs for channel 9 (middle panel). Unlike the higher vibrational levels, the lower ones are quenched by O$_2$ at a much slower rate (see Table 1 of Panka et al., 2017) and, therefore, reaction (2) plays here a more important role.

By taking the ratio between the VERs, we find that they are (nearly) linearly dependent on the O(^{3}P) density (right panel of Figure 1). The various VER slopes displayed in this panel are the result of different relative contributions of various mechanisms (i.e., collisional and radiative) influencing OH(v) populations at different pressures.

The right panel of Figure 1 also shows that VER ratios demonstrate very different slopes for each pressure level when reaction (2) is turned on and off. The VER ratio slopes increase strongly when reaction (2) is turned on because channel 9 VERs are getting to be far more sensitive to the O(^{3}P) compared to those of channel 8 as discussed above.

The linear relationship seen in Figure 1 provides the basis for a simple but robust algorithm for retrieving O(^{3}P) from SABER OH radiances used in this study. A simple iterative forward-fit routine exploiting the linearity shown in the right panel of Figure 1 requires at each altitude three iterations to fit the VER ratio of the measured signals with the calculated ratio using the local O(^{3}P) volume mixing ratio (VMR) as a fitting parameter. In combination with the fast solution of (1) as a local problem, the new algorithm allows processing a large volume of data without any simplifying assumptions in the non-LTE modeling, which guarantees a high quality of retrieved results.

The new retrieval approach improves upon the commonly used method for retrieving atomic oxygen (see Mlynczak et al., 2013; Smith et al., 2010, and references therein) by eliminating its corner stone assumptions about main processes of ozone quenching entering into the chemical balance equation and about the validity of the ozone chemical equilibrium, which are not always true in the mesopause region (see Belikovich et al., 2018; Kulikov et al., 2017, 2018).

One may also see in Figure 1, right panel, that O(^{3}P) VMRs retrieved with this algorithm are, however, dramatically different when reaction (2) is turned on or off: retrieved O(^{3}P) VMRs will be roughly higher by a factor of 2 for the same measured VER ratios when reaction (2) is off. These unrealistically high retrievals will dramatically exceed O(^{3}P) obtained from any other observations. In contrast, the presence of reaction (2) in the model brings the retrieved O(^{3}P) in agreement with other observations. We show this in the next section.

3. Results and Discussion

The retrieved O(^{3}P) presented below (hereafter [O]-2018) relies on the nighttime OH VERs for the SABER channels 8 and 9, atmospheric pressures, and temperatures, retrieved for the same scans, as well as N$_2$/O$_2$ densities which were all taken from the current SABER Level2 V2.0 database.

Figure 2 shows comparisons between SABER-2013, OSIRIS, SCIAMACHY, WINDII, and [O]-2018 mean retrievals for the 20°–40°N and 40°–60°N latitudinal bands on September 2005. Uncertainties in the mean retrieved atomic oxygen are displayed for SABER-2013 ($\pm$20%) following Mlynczak et al. (2013) and for SCIAMACHY ($\pm$15%) from Kaufmann et al. (2014). The total errors of [O]-2018 in Figure 2 depend on the altitude and vary within $\pm$(25–27)%. They were estimated by accounting for the SABER instrument random noise and uncertainties of the non-LTE model parameters and atmospheric inputs. It can be seen in both panels of Figure 2 that the mean [O]-2018 is typically lower than SABER-2013 by 20–50% between 88 and 100 km.

In addition, it is shown in Figure 2 that, unlike the SABER-2013 results, the [O]-2018 mean retrievals agree with the results of previous independent observations. Specifically, the [O]-2018 retrievals agree with the SCIAMACHY results within the error bars in the range 88–100 km. Below 88 km both [O]-2018 retrievals and those of SCIAMACHY decrease with decreasing altitude; however, [O]-2018 retrievals are higher, reaching values $\approx 1.5 \times 10^{11}$ atoms/cm^3 at 85 km compared to $\approx 0.8 \times 10^{11}$ atoms/cm^3 for SCIAMACHY. O(^{3}P) derived
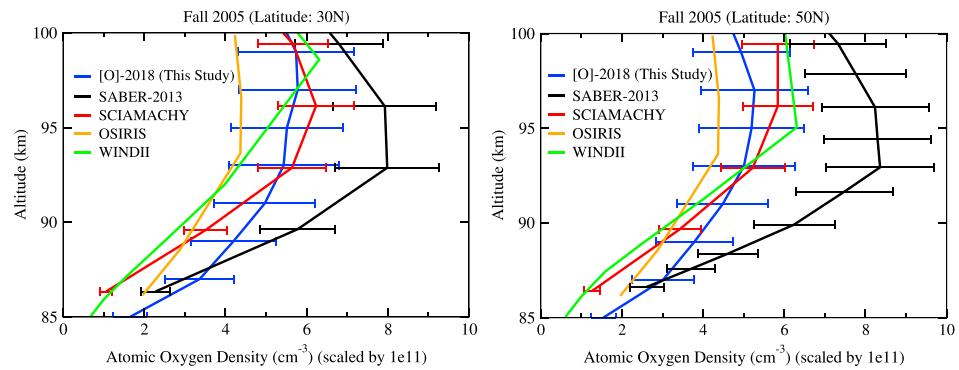
Figure 2. Zonal mean atomic oxygen density for Fall 2005 at (left) 20°–40°N and (right) 40°–60°N. Results for SABER-2013, SCIAMACHY, and OSIRIS are taken from Kaufmann et al. (2014). Results for WINDII are taken from Russell et al. (2005). SABER = Sounding of the Atmosphere using Broadband Emission Radiometry; SCIAMACHY = Scanning Imaging Absorption Spectrometer for Atmospheric Chartography; OSIRIS = Optical Spectrograph and Infrared Imager System; WINDII = WIND Imaging Interferometer.

from WINDII also overlap with [O]-2018 retrievals above 92 km in Figure 2 (left) and above 89 km in Figure 2 (right). Below these altitudes, however, WINDII results are lower than [O]-2018 retrievals and, at some altitudes, slightly lower than SCIAMACHY. O(^{3}P) densities derived from OSIRIS measurements are about 10% lower than SCIAMACHY and [O]-2018 retrievals above 90 km but fall within the error bars of other measurements below this altitude.

4. Conclusion

Based on a new detailed non-LTE OH(v) model described by Panka et al. (2017), we retrieve O(^{3}P) densities in the range of 85–100 km from the SABER nighttime limb measurements of OH(v) Meinel band emissions at 2.0 and 1.6 μms.

We demonstrate that the OH(v)+O(^{3}P) mechanism (2) proposed by Sharma et al. (2015) plays a key role in the formation of OH Meinel band emissions as well as in retrieving adequate O(^{3}P) densities. Using this mechanism, there is no need for the empirically lowered quenching rate of the OH(v)+O(^{3}P) reaction used in Mlynczak et al. (2013) for modeling the SABER radiances. The new kinetic OH(v) model accurately predicts the relative SABER OH VERs using the measured quenching rates and, furthermore, yields O(^{3}P) retrievals which provide good agreement with the measurements of WINDII, OSIRIS, and SCIAMACHY (Kaufmann et al., 2014). In addition, it has been demonstrated in Panka et al. (2017) that the new OH(v) kinetic model can seamlessly explain the nighttime CO$_2$ 4.3-μm radiance enhancements, without any empirical adjustment of collisional rates.

Our results provide a critical step forward in the understanding of the MLT physics and chemistry and solve a historical discrepancy regarding the amount of O(^{3}P) in the nighttime MLT. It also causes the reestimation of both chemical heating and radiative cooling of this region. Chemical heating of the MLT is dominated by recombination reactions O+O+M→O$_2$+M and O+O$_2$+M→O$_3$+M as well as the OH production H+O$_3$ →OH+O$_2$ and loss OH+O→ H+O$_2$ reactions (Mlynczak & Solomon, 1993). Three of them directly involve O atoms. On the other hand, the strongest radiative cooling of this region is caused by the CO$_2$ 15-μm emission generated by collisions CO$_2$ molecules with O atoms (Brasseur & Solomon, 2005). In Figure 3 we show how the mean chemical heating and CO$_2$ cooling change depending whether SABER-2013 or [O]-2018 is used. Using [O]-2018, which is 20% to 50% lower than SABER-2013, reduces the mean chemical heating around the mesopause by 10 K/day and the mean radiative cooling by the CO$_2$ 15-μm radiation by 2 K/day. This will bring the global annual chemical heating, which was extremely high for SABER-2013,
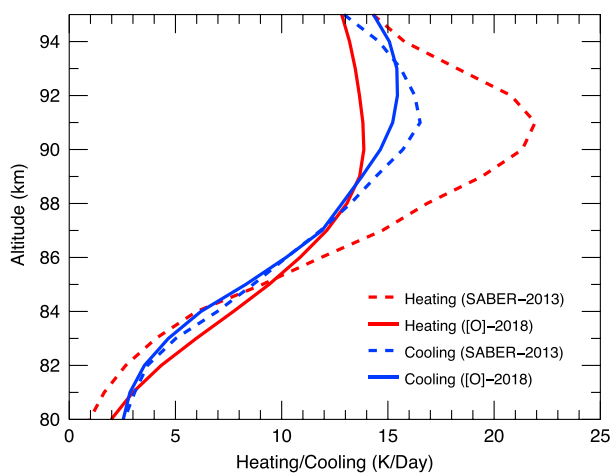

Figure 3. Mean chemical heating (red) and the 15-μm CO$_2$ cooling (blue) rates for the night of 27 September 2005. Dash and solid profiles represent SABER-2013 and [O]-2018, respectively. SABER = Sounding of the Atmosphere using Broadband Emission Radiometry.

into a better agreement with the global radiative cooling. Massive O(^{3}P) retrievals, which follow this study, will allow investigating the spatial and temporal variabilities of O(^{3}P) as well as chemical heating and radiative cooling in the MLT at different scales. This will enable the study of long-term trends, benefiting, compared to other observations, from a broad coverage and unprecedented duration (more than 16 years) of SABER observations.

References

Belikovich, M. V., Kulikov, M. Y., Grygalashvyly, M., Sonnemann, G. R., Ermakova, T. S., Nechaev, A. A., & Feigin, A. M. (2018). Ozone chemical equilibrium in the extended mesopause under the nighttime conditions. *Advances in Space Research*, *61*, 426–432. https://doi.org/10.1016/j.asr.2017.10.010

Brasseur, G. P., & Solomon, S. (2005). *Aeronomy of the middle atmosphere: Chemistry and physics of the stratosphere and mesosphere* (3rd ed). Dordrecht, Netherlands: Springer Science & Business Media.

Cosby, P. C., & Slanger, T. G. (2007). OH spectroscopy and chemistry investigated with astronomical sky spectra. *Canadian Journal of Physics*, *85*, 77–99. https://doi.org/10.1139/P06-088

Feofilov, A. G., & Kutepov, A. A. (2012). Infrared radiation in the mesosphere and lower thermosphere: Energetic effects and remote sensing. *Surveys in Geophysics*, *33*, 1231–1280. https://doi.org/10.1007/s10712-012-9204-0

Gusev, O. A., & Kutepov, A. A. (2003). Non-LTE gas in planetary atmospheres. In I. Hubeny, D. Mihalas & K. Werner (Eds.), *Stellar atmosphere modeling, Astronomical Society of the Pacific Conference Series* (Vol. 288, pp. 318–330). San Francisco, CA: Astronomical Society of the Pacific.

Kalogerakis, K. S., Matsiev, D., Sharma, R. D., & Wintersteiner, P. P. (2016). Resolving the mesospheric nighttime 4.3 μm emission puzzle: Laboratory demonstration of new mechanism for OH(v) relaxation. *Geophysical Research Letters*, *43*, 8835–8843. https://doi.org/10.1002/2016GL069645

Kalogerakis, K. S., Smith, G. P., & Copeland, R. A. (2011). Collisional removal of OH(X $^2\Pi$, $v = 9$) by O, O$_2$, O$_3$, N$_2$, and CO$_2$. *Journal of Geophysical Research*, *116*, D20307. https://doi.org/10.1029/2011JD015734

Kaufmann, M., Gusev, O. A., Grossmann, K. U., Martín-Torres, F. J., Marsh, D. R., & Kutepov, A. A. (2003). Satellite observations of daytime and nighttime ozone in the mesosphere and lower thermosphere. *Journal of Geophysical Research*, *108*, 4272. https://doi.org/10.1029/2002JD002800

Kaufmann, M., Zhu, Y., Ern, M., & Riese, M. (2014). Global distribution of atomic oxygen in the mesopause region as derived from SCIAMACHY O(^{1}S) green line measurements. *Geophysical Research Letters*, *41*, 6274–6280. https://doi.org/10.1002/2014GL060574

Kulikov, M. Y., Belikovich, M. V., Grygalashvyly, M., Sonnemann, G. R., Ermakova, T. S., Nechaev, A. A., & Feigin, A. M. (2017). Daytime ozone loss term in the mesopause region. *Annales Geophysicae*, *35*, 677–682. https://doi.org/10.5194/angeo-35-677-2017

Kulikov, M. Y., Belikovich, M. V., Grygalashvyly, M., Sonnemann, G. R., Ermakova, T. S., Nechaev, A. A., & Feigin, A. M. (2018). Nighttime ozone chemical equilibrium in the mesopause region. *Journal of Geophysical Research: Atmospheres*, *123*, 3228–3242. https://doi.org/10.1002/2017JD026717

Kutepov, A. A., Feofilov, A. G., Marshall, B. T., Gordley, L. L., Pesnell, W. D., Goldberg, R. A., & Russell, J. M. (2006). SABER temperature observations in the summer polar mesosphere and lower thermosphere: Importance of accounting for the CO$_2$ v_2 quanta V-V exchange. *Geophysical Research Letters*, *33*, L21809. https://doi.org/10.1029/2006GL026591

Kutepov, A. A., Gusev, O. A., & Ogibalov, V. P. (1998). Solution of the non-LTE problem for molecular gas in planetary atmospheres: Superiority of accelerated lambda iteration. *Journal of Quantitative Spectroscopy and Radiative Transfer*, *60*, 199–220. https://doi.org/10.1016/S0022-4073(97)00167-2

López-Puertas, M., & Taylor, F. W. (2001). *Non-LTE radiative transfer in the atmosphere* (Vol. 3). Singapore: World Scientific.

Marsh, D. R., Mills, M. J., Kinnison, D. E., Lamarque, J.-F., Calvo, N., & Polvani, L. M. (2013). Climate change from 1850 to 2005 simulated in CESM1 (WACCM). *Journal of Climate*, *26*(19), 7372–7391.

Migliorini, A., Gérard, J. C., Soret, L., Piccioni, G., Capaccioni, F., Filacchione, G., et al. (2015). Terrestrial OH nightglow measurements during the Rosetta flyby. *Geophysical Research Letters*, *42*, 5670–5677. https://doi.org/10.1002/2015GL064485

Mlynczak, M. G., Hunt, L. A., Mast, J. C., Thomas Marshall, B., Russell, J. M., Smith, A. K., et al. (2013). Atomic oxygen in the mesosphere and lower thermosphere derived from SABER: Algorithm theoretical basis and measurement uncertainty. *Journal of Geophysical Research: Atmospheres*, *118*, 5724–5735. https://doi.org/10.1002/jgrd.50401

Mlynczak, M. G., & Solomon, S. (1993). A detailed evaluation of the heating efficiency in the middle atmosphere. *Journal of Geophysical Research*, *98*(D6), 10,517–10,541.

Panka, P. A., Kutepov, A. A., Kalogerakis, K. S., Janches, D., Russell, J. M., Rezac, L., et al. (2017). Resolving the mesospheric nighttime 4.3 μm emission puzzle: Comparison of the CO$_2$(v_3) and OH(v) emission models. *Atmospheric Chemistry & Physics*, *17*, 9751–9760. https://doi.org/10.5194/acp-17-9751-2017

Russell, J. P., Ward, W. E., Lowe, R. P., Roble, R. G., Shepherd, G. G., & Solheim, B. (2005). Atomic oxygen profiles (80 to 115 km) derived from Wind Imaging Interferometer/Upper Atmospheric Research Satellite measurements of the hydroxyl and greenline airglow: Local time-latitude dependence. *Journal of Geophysical Research*, *110*, D15305. https://doi.org/10.1029/2004JD005570

Sharma, R. D., Wintersteiner, P. P., & Kalogerakis, K. S. (2015). A new mechanism for OH vibrational relaxation leading to enhanced CO$_2$ emissions in the nocturnal mesosphere. *Geophysical Research Letters*, *42*, 4639–4647. https://doi.org/10.1002/2015GL063724

Sheese, P. E., McDade, I. C., Gattinger, R. L., & Llewellyn, E. J. (2011). Atomic oxygen densities retrieved from Optical Spectrograph and Infrared Imaging System observations of O$_2$ A-band airglow emission in the mesosphere and lower thermosphere. *Journal of Geophysical Research*, *116*, D01303. https://doi.org/10.1029/2010JD014640

Smith, A. K., Marsh, D. R., Mlynczak, M. G., & Mast, J. C. (2010). Temporal variations of atomic oxygen in the upper mesosphere from SABER. *Journal of Geophysical Research*, *115*, D18309. https://doi.org/10.1029/2009JD013434

Smith, A. K., Marsh, D. R., Russell, J. M., Mlynczak, M. G., Martin-Torres, F. J., & Kyrölä, E. (2008). Satellite observations of high nighttime ozone at the equatorial mesopause. *Journal of Geophysical Research*, *113*, D17312. https://doi.org/10.1029/2008JD010066

Xu, J., Gao, H., Smith, A. K., & Zhu, Y. (2012). Using TIMED/SABER nightglow observations to investigate hydroxyl emission mechanisms in the mesopause region. *Journal of Geophysical Research*, *117*, D02301. https://doi.org/10.1029/2011JD016342